CrossMark

A Hale-like Cycle in the Solar Twin 18 Scorpii

J.-D. do Nascimento, Jr.[1,2], S. A. Barnes[3], S. H. Saar[1], G. F. Porto de Mello[4], J. C. Hall[5], F. Anthony[2],
L. de Almeida[6], E. N. Velloso[2], J. S. da Costa[2], P. Petit[7], A. Strugarek[8], B. J. Wargelin[1], M. Castro[2],
K. G. Strassmeier[3], and A. S. Brun[8]

[1] Center for Astrophysics, Harvard & Smithsonian, 60 Garden Street, Cambridge, MA 02138, USA; jdonascimento@cfa.harvard.edu
[2] Dep. de Física, Univ. Federal do Rio Grande do Norte—UFRN, Natal, RN, 59078-970, Brazil
[3] Leibniz-Institut für Astrophysik Potsdam (AIP), An der Sternwarte 16, D-14482, Potsdam, Germany
[4] Observ. do Valongo, Univ. Federal do Rio de Janeiro—UFRJ, Ladeira do Pedro Antonio 43, RJ, 20080-090, Brazil
[5] Lowell Observatory, 1400 West Mars Hill Road, Flagstaff, AZ 86001, USA
[6] Laboratório Nacional de Astrofísica, Rua Estados Unidos 154, 37504-364, Itajubá—MG, Brazil
[7] Institut de Recherche en Astrophysique et Planétologie, Univ. de Toulouse, CNRS, CNES, F-31400, Toulouse, France
[8] Dép. d'Astrop./AIM, CEA/IRFU, CNRS/INSU, Univ. Paris-Saclay & Univ. Cité de Paris, F-91191 G.sur-Yvette, France

Abstract

Characterizing the cyclic magnetic activity of stars that are close approximations of our Sun offers our best hope for understanding our Sun's current and past magnetism, the space weather around solar-type stars, and more generally, the dynamos of other cool stars. The nearest current approximation to the Sun is the solar twin 18 Scorpii, a naked-eye Sun-like star of spectral type G2 Va. However, while 18 Scorpii's physical parameters closely match those of the Sun, its activity cycle is about 7 yr, and shorter than the solar cycle. We report the measurement of a periodicity of 15 yr that corresponds to a longer activity cycle for 18 Scorpii based on observations extending to the last three decades. The global magnetic geometry of 18 Scorpii changes with this 15 yr cycle and appears to be equivalent to the solar 22 yr magnetic polarity cycle. These results suggest that 18 Scorpii is also a magnetic proxy for a younger Sun, adding an important new datum for testing dynamo theory and magnetic evolution of low-mass stars. The results perturb our understanding of the relationship between cycle and rotation, constrain the Sun's magnetism and the Sun–Earth connection over the past billion years, and suggest that solar Schwabe and Hale cycle periods have increased over that time span.

Unified Astronomy Thesaurus concepts: Solar cycle (1487); Stellar evolution (1599); Stellar magnetic fields (1610); Solar analogs (1941); Spectropolarimetry (1973)

1. Introduction

Understanding the nature of the solar dynamo, the mechanism by which the magnetic field of the Sun is regularly amplified, sustained, and lost, remains one of the most challenging questions in astrophysics (Charbonneau 2010; Hathaway 2015; Brun & Browning 2017). A ∼10 yr cycle for the Sun was first suggested after a 17 yr long study of sunspots 170 yr ago (Schwabe 1843). Several decades later, polarimetric observations revealed a relationship between sunspots and magnetic activity, in particular, that the Sun's global magnetic field had opposite polarities in consecutive cycles (Hale et al. 1919). The Hale magnetic cycle is thus twice as long as the Schwabe chromospheric cycle.

In fact, by combining historical records of the sunspot number, the variabilities of the solar cycle are now better understood. This cycle is observed to vary both in strength (up to a factor of 2.5 in the sunspot number) and length (up to 27%). We also know that odd cycles tend to be more intense than even cycles, which is known as the empirical Gnevyshev–Ohl rule, as illustrated in Figure 1 (Hathaway 2015).

Pioneering work since 1966 by Wilson (1968, 1978) and successors has shown that many stars exhibit chromospheric cycles with different periods, amplitudes, and shapes. These properties seem to be controlled by various stellar parameters, a major ingredient of which is thought to be differential rotation. Specifically, according to dynamo models, activity variations in the solar magnetic field are a consequence of the interplay between cyclonic convection and differential rotation, which generates a large-scale toroidal magnetic field from an initial poloidal field, and subsequently regenerates the poloidal field from the toroidal, hence closing the dynamo loop (Parker 1955; Babcock 1961; Leighton 1969; Dikpati et al. 2004; Strugarek et al. 2017; Brun et al. 2022). A comparison between activity cycle properties of similar stars at different evolutionary stages is essential to understand how dynamo ingredients slightly different from the Sun can influence the overall magnetic activity behavior of solar-type stars. Unfortunately, of the initial Mount Wilson sample spanning the broad range of spectral types F to K, no star was found to be a good proxy for the Sun in terms of its fundamental parameters.

Activity cycle measurement campaigns recognized the need to characterize G-type stars of solar mass and fundamental parameters within 10% of the solar values (Table 1) only after the term "solar spectral analogs" was coined in 1978 (Hardorp 1978) and "solar twin" in 1996 (Cayrel de Strobel 1996). A star would be a solar twin if the determined physical parameters (e.g., mass, effective temperature, age, and metallicity) were identical to those of the Sun, and if the star were spectroscopically indistinguishable from the Sun. Soon thereafter, 18 Scorpii (18 Sco, HR 6060, or HD 146233) was identified as the best solar twin via high-resolution spectroscopy and supporting data (Porto de Mello & da Silva 1997). In fact, 18 Sco exhibits the smallest deviations in effective
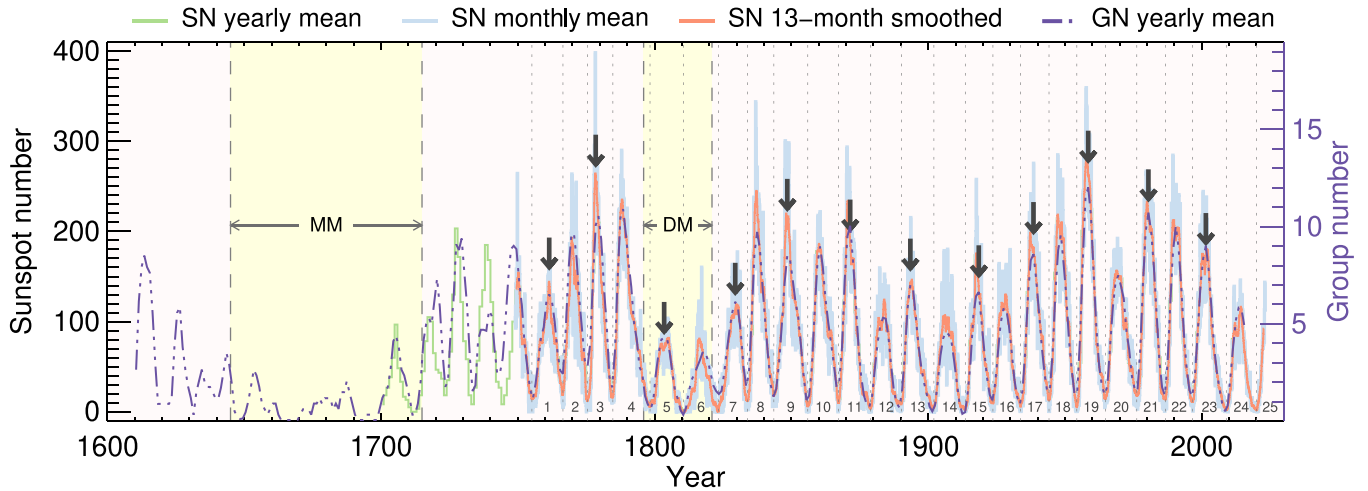
Figure 1. The historical sunspot number record smoothed by yearly averages. MM and DM indicate the time periods of the so-called Maunder Minimum and Dalton Minimum, respectively. The odd-cycle maxima are highlighted with arrows to help visualize the Gnevyshev–Ohl pattern. Sunspots were observed avidly with telescopes soon after Galileo called attention to their existence in the Western world. From a historical perspective, we note that if the telescope had been invented about 100 yr later, the Maunder Minimum episode would have been missed entirely.

Table 1
Physical Properties of 18 Sco

Parameters	18 Sco	Sun
T_{eff} (K) (1), (2)	5817 ± 4	5772 ± 0.8
$\log g_{\star}$ (cgs) (1), (2)	4.448 ± 0.012	4.438 ± 0.001
[Fe/H] (dex) (1)	0.052 ± 0.005	0.0
$R_{\star}$ ($R_{\odot}$) (3)	1.010 ± 0.009	1.0
$M_{\star}$ ($M_{\odot}$) (1)	1.03 ± 0.03	1.0
Age (Gyr) (4), (5), (6)	$3.36^{+0.52}_{-0.52}$; $3.66^{+0.44}_{-0.50}$	4.57 ± 0.11
P_{rot} (days) (7)	22.7 ± 0.5	25.4 ± 1.0
$\langle S_{\text{MW}} \rangle$ (8)	$0.172 \pm 0.007^{\text{a}}$	0.1701 ± 0.0005
$L_{\star}$ ($L_{\odot}$) (1)	1.0438 ± 0.012	1.0

Note.
[a] This study.
References. (1) Bazot et al. (2018), (2) Mamajek et al. (2015), (3) Bazot et al. (2011), (4) Meléndez et al. (2014), (5) Li et al. (2012), (6) Bonanno et al. (2002), (7) Petit et al. (2008), (8) Egeland et al. (2017).

temperature, surface gravity, luminosity, metallicity, and UBV colors when compared to solar values (Table 1); due to its slightly younger age, it could also be referred to as a "solar doppelgänger." Crucially, it is the brightest ($V = 5.51$) and nearest (13.9 pc) solar twin (Porto de Mello & da Silva 1997; Soubiran & Triaud 2004; Takeda et al. 2007; Datson et al. 2012, 2014; Porto de Mello et al. 2014). Furthermore, its brightness and decl. ($-8°$) allows it to be observed from both the northern and southern hemispheres with a variety of techniques. Consequently, 18 Sco has been a major target for a wide variety of astrophysical studies (Luck & Heiter 2005; Hall et al. 2007; Petit et al. 2008; Trilling et al. 2008; Ramírez et al. 2009; Tanner et al. 2010; Bazot et al. 2011, 2012; Meléndez et al. 2014) and is crucial to investigating the solar-stellar connection (Strassmeier 2004).

In particular, these studies report a slightly higher Li abundance and faster rotation as compared with the Sun, indicating that 18 Sco is somewhat younger (3.4–3.7 Gyr old), and thus represents the Sun's behavior 0.9–1.2 Gyr ago. High-precision differential photometry shows brightness changes of less than 0.09%, and chromospheric Ca II measurements reveal a solar-like activity cycle with a period of ∼7 yr and an

amplitude of ∼10% (Hall et al. 2007). 18 Sco thus suggests that stars extremely similar to the Sun in their fundamental, basic photospheric, spectroscopic, chromospheric, coronal, and evolutionary properties should share activity and magnetic patterns that are also remarkably similar to the Sun. In practical terms, in addition to the chromospheric cycle, the Sun has a longer magnetic cycle, one not yet observed in 18 Sco, and represents an anthropic asymmetry. At the same time, identifying and then adequately monitoring solar twins would take at least three decades to obtain similar results. The past four decades of observations of 18 Sco, together with the fact that this solar proxy is currently undergoing a phase of maximum activity, provide a unique opportunity to better characterize 18 Sco in terms of its magnetic cycle and to examine whether the Sun is an outlier or otherwise unique, shedding further insight on the solar-stellar connection.

The remaining parts of this paper are organized as follows: In Section 2 we define our time-series data set by detailing all the calibration and reduction procedures. Next, Section 3 details our ensemble of multicomponent analysis methods. We then examine in greater depth the historical age estimates for 18 Scorpii in Section 4. In Section 5 we discuss and interpret our findings within the overall context of stellar cycles, and we summarize our conclusions in Section 6.

2. Spectroscopic and Polarimetric Observations and Data Reduction

The standard indicator of chromospheric activity is the *S*-index (Wilson 1968), which is extracted from measures of the emission-line cores of the Ca II H and K lines. All Ca II H and K core emission measurements were converted into normalized *S*-indices on the Mount Wilson Observatory (MWO) scale. We performed quality diagnostics to individually filter out poor spectra (see Figure 2). In addition to acquiring dedicated new spectroscopic observations at Pico dos Dias Observatory (OPD), we collected and recalibrated a long series of prior observations. For High-Accuracy Radial-velocity Planet Searcher (HARPS; Mayor et al. 2003), NARVAL (Aurière 2003), and Spectrograph for Observation of PHenomena in stellar Interior and Exoplanets (SOPHIE;
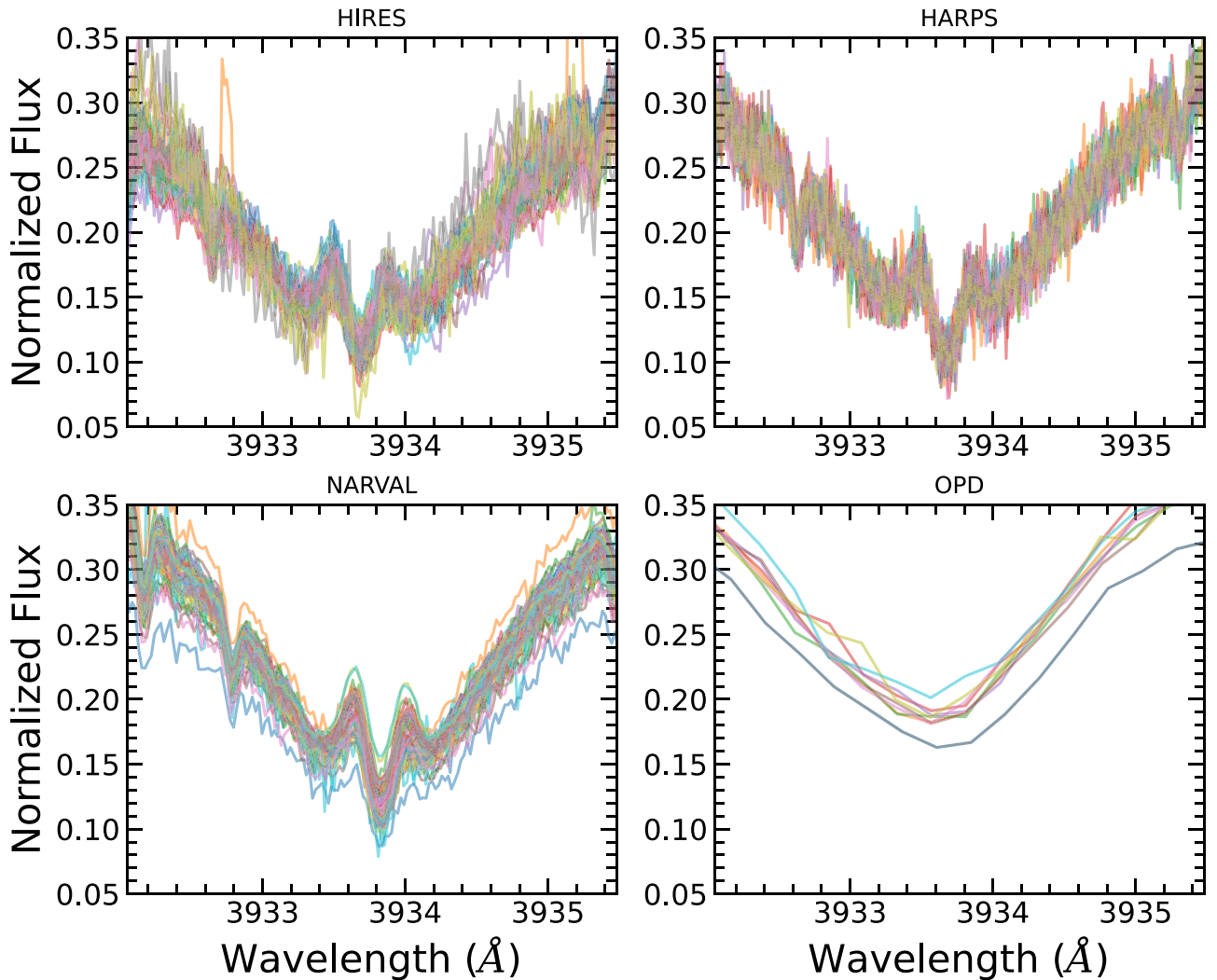
Figure 2. Overplotted spectra of 18 Sco in the K-line region for each instrument. The colors represent individual spectra for visualization purposes. For instruments with more than 50 spectra in their final sample, only 50 are shown in the plot. Top left—HIRES (250 total spectra). Top right—HARPS (2716 total spectra). Bottom left—NARVAL (70 total spectra). Bottom right—OPD (31 total spectra).

Bouchy & Sophie Team [2006]), we reduced, normalized, and filtered all spectra before computing the instrumental S-index. All High Resolution Echelle Spectrometer (HIRES; Vogt et al. [1994]) spectra were filtered, and most of them showed numerous instrumental anomalies near the Ca II H and K regions. We used the S_{MW} measurements for the Mount Wilson and Lowell data. The OPD data were acquired and reduced by us. Next, we show how the final values of S_{MW} were derived for each instrument.

2.1. HARPS

Before computing the instrumental S-index for all HARPS spectra, we corrected for the radial velocity and applied three filters to the data set. The first filter followed the prescription presented by Wright et al. ([2004]), where the authors outline a method for diagnosing the extraction quality of the S-index by modeling the dependence of the H/K on the obtained S-index. We applied a spline function to this correlation and set a 10% threshold to retain only the spectra with good correlation.

The second filter took the error bar of the S-index measurements into account. To do this, we computed the S-index with the spectra summed with its superior error, and then

again with the inferior error. Thus we have the S-index for the superior and inferior errors. To find the final error, we evaluated $\mathrm{err}_+ = |S - S_{\mathrm{err}_+}|$ and $\mathrm{err}_- = |S - S_{\mathrm{err}_-}|$. Then, the mean error is $\mathrm{err} = (\mathrm{err}_+ + \mathrm{err}_-)/2$.

The two previous steps filter the majority of spectra without any need for visual inspection, but some poor spectra are still left in the data set. As we had 5532 spectra to visually inspect, we simply plotted all spectra together and saw that all poor spectra presented noise lines with flux values lower than 0.045 (after normalization) between 393.31 and 393.36 nm. The third filter then eliminated all spectra that presented a normalized flux lower than 0.045 between 393.31 and 393.36 nm.

After applying the first and second filters, we eliminated 126 spectra. After the third filter, we were left with a sample of 2716 final spectra (overplotted in the top right panel of Figure 2).

With the final sample, we followed the prescription of Duncan et al. ([1991]) to mimic the response of the Mount Wilson HKP-2 spectrophotometer. We took a triangular bandpass at the core of the H and K lines at 3968.47 Å and 3933.664 Å, respectively, and two 20 Å wide rectangular bandpasses to measure the nearby continuum; V centered on 3901.07 Å and R centered on 4001.07 Å. The equation is given

as

$$S_{\text{HARPS}} = 8\alpha \frac{N_H + N_K}{N_V + N_R}, \quad (1)$$

where N_H, N_K, N_V, and N_R are the counts of the respective bandpasses, 8 is a correction factor for the longer exposure times of the V and R bandpasses of the HKP-2 instrument, and α is a proportionality constant, usually taken to be $\alpha = 2.4$. We calibrated S_{HARPS} to S_{MW} by performing a linear regression on stars common in both surveys. Even though the observations are not contemporaneous, the small S-index variance ($\lesssim 1\%$) in the time series allows us to define

$$S_{\text{MW}} = aS_{\text{HARPS}} + b, \quad (2)$$

where $a = 1.1159$ and $b = 0.0343$.

2.2. HIRES

The initial sample for HIRES spectra had 342 spectra. The same procedure as we used on HARPS spectra was performed for the HIRES spectra. We corrected for radial velocity and visually inspected each spectrum to eliminate poor spectra. Our final sample was then 250 spectra (shown in the top left panel of Figure 2). We then computed the instrumental S-index following the same procedure as for the HARPS spectra and transformed it into the S-index of Mount Wilson using $S_{\text{MW}} = 17S_{\text{HIRES}} + 0.063$.

2.3. SOPHIE

All 18 Sco SOPHIE spectra were directly retrieved from The SOPHIE Archive[9] and were reduced in the same way as the HARPS spectra. We normalized, corrected for radial velocity, and visually inspected the Ca II H and K regions. The instrumental S-index was calculated in the same way as S_{MW} (Baliunas et al. 1995)

$$S_{\text{SOPHIE}} = \frac{H + K}{B + V}, \quad (3)$$

where H and K are triangular windows centered at 3968.47 Å and 3933.664 Å, respectively, and V and B are two 20 Å wide rectangular bandpasses to measure the nearby continuum; B centered on 3900 Å and V centered on 4000 Å. In order to mimic the S_{MW}, we applied the normalization equation $S_{\text{MW}} = 0.07S_{\text{SOPHIE}} + 0.16$.

2.4. OPD

The spectra obtained at the Pico dos Dias Observatory (OPD) underwent the same procedures as the other instruments. To calibrate the S_{MW} from OPD, we applied calibration equations for two different detectors used in the OPD COUDÉ spectrograph. The calibration was performed by applying a spline to the compared values of 26 Mount Wilson standard stars. In addition to the detector, all observations followed the same instrumental setup. Thus, we used two different calibrations for the coudé spectra,

$$S_{\text{MW}} = 8.629S_{\text{COUDE1}} - 0.11, \quad (4)$$

$$S_{\text{MW}} = 4.239S_{\text{COUDE2}} + 0.024, \quad (5)$$

where S_{COUDE1} and S_{COUDE2} are the spectra obtained with the two detectors. In Figure 2 we overplot 31 spectra that have a lower resolution than those from the other instruments. This lower resolution is reflected in larger uncertainties in the S-index values.

2.5. Mount Wilson and Lowell

We obtained S-index measurements from the HK project at the Mount Wilson Observatory,[10] and the observation and reduction procedure was described in detail by Vaughan et al. (1978). The Lowell measurements were already calibrated for S_{MW} and were obtained via private communication with the responsible observer.

2.6. NARVAL

We reduced 92 NARVAL spectra for 18 Sco using the ".s" and ".out" files. We corrected the radial velocity for telluric lines (km s^{-1}) with information found in the ".out" files. Some spectra were too far out in wavelength to correct, so we eliminated 17 spectra. After this, we visually inspected all 75 spectra to eliminate those that presented a poor signal or instrumental anomalies near the Ca II H and K regions. We then ended up with 70 valid spectra (50 are shown in the bottom left panel of Figure 2). For NARVAL, we note that all H regions presented anomalies and discontinuities. To avoid the problem of using problematic H regions, we computed the instrumental S-index simply as $S_{\text{NARVAL}} = N_K/N_V$ with $N_K = 3933.68$ Å and $N_V = 3901.07$ Å following the same width as HARPS.

To mimic the S_{MW}, as we have S_{HARPS} converted into S_{MW} with contemporaneous observations, we adjusted the instrumental S_{NARVAL} to the tendency of the S_{MW} temporal series with a linear slope $S_{\text{MW}} = S_{\text{NARVAL}} + 0.03$.

2.6.1. 18 Sco Spectropolarimetric Magnetic Measurements

18 Sco was monitored by ESPaDOnS and NARVAL from 2005 to 2019, with a total of 70 circularly polarized (Stokes V) observations collected over this period. The log of these observations is presented in Table 5. The amplitude of polarized Zeeman signatures of low-activity Sun-like stars is much smaller than the photon noise when individual spectral lines are considered. To obtain a statistical improvement of this situation, we applied the least-squares deconvolution method to extract an average pseudo-line profile from a list of photospheric lines (Donati et al. 1997; Kochukhov et al. 2010), repeating here the procedure adopted for this target by Petit et al. (2008).

In the majority of the observations, no Zeeman signature was detected according to the detection criterion of Donati et al. (1997), i.e., no signal recorded with a false-alarm probability lower than 10^{-5}. The longitudinal projection of the magnetic field was then computed according to the first moment of the Stokes V LSD profile,

$$B_{\text{eff}} = -2.14 \times 10^{-11} \frac{\int vV(v)dv}{\lambda_0 g_{\text{eff}} c \int (1 - I(v))dv} \, G. \quad (6)$$

---

[9] http://atlas.obs-hp.fr

[10] Located at Mount Wilson, at 1742 m altitude in the San Gabriel Mountains, LA, California, the observatory has two telescopes: the Hale telescope (1.5 m), built in 1908, and the Hooker telescope (2.5 m), built in 1917.
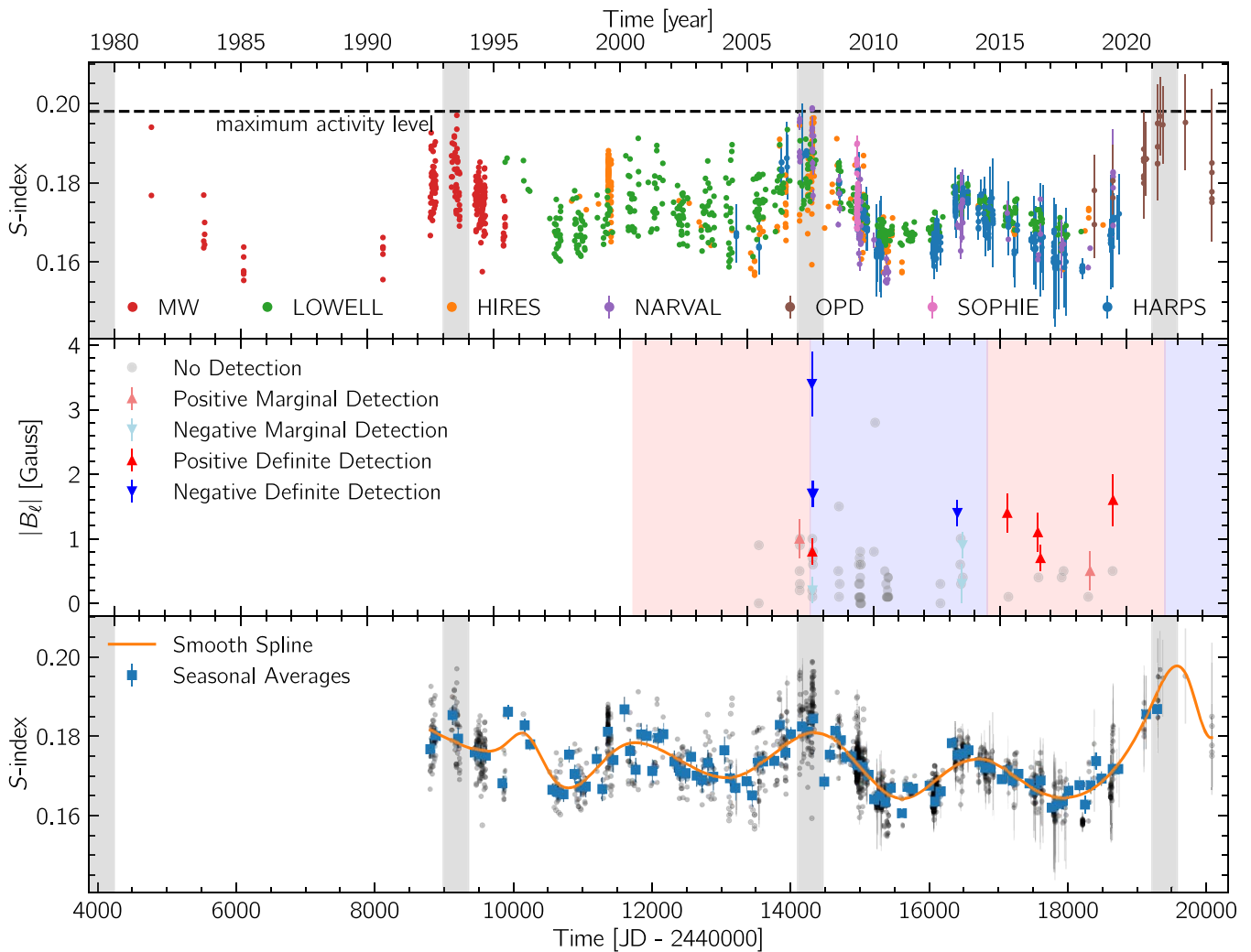
Figure 3. Summary of observational data for 18 Sco. The light gray stripes indicate the approximate regions of magnetic maxima spaced at ≈ 15 yr intervals. Top panel—calibrated S-index measurements taken from seven different sources. The horizontal dashed line indicates the maximum measured activity level in this period. Middle panel—spectropolarimetric observations of the magnetic field. The red and blue backgrounds represent the expected polarities for a ≈ 15 yr magnetic cycle. Bottom panel—differing levels of processing applied to the original S-index time series for each analysis: last 30 yr (gray circles), seasonal averages (blue squares), and smoothed interpolation (orange line).

In this equation, I and V are the Stokes I and V LSD profiles, respectively, v is the radial velocity (in km s^{-1}), λ_0 is the central wavelength of the LSD line profile (equal to 650 nm), and g_{eff} is the effective Landé factor (equal to 1.05).

The middle panel of Figure 3 shows the measured magnetic flux during this period. Following the detection criterion, and depending on the noise pattern, a nondetection can still lead to a nonzero longitudinal field. Only a few dates provided us with a firmly detected signal. Three of them were in 2007, close to an S-index maximum of the star, although the weakness and the geometrical complexity of the magnetic field prevented us from detecting Zeeman signatures at all rotational phases. A Zeeman–Doppler imaging (ZDI) map was reconstructed from this subset of observations (Petit et al. 2008), and the global modeling of the subset was successful at extracting useful information from rotation phases with a signal lower than but close to the detection limit. The lack of a dominant field polarity in this timeframe can suggest a transition between more stable configurations. Indeed, observations of the Sun and of the cool solar-type star 61 Cyg A close to activity minima (Sanderson et al. 2003; Boro Saikia et al. 2016, 2018a) suggest

that their global field can adopt a simpler, more axisymmetric, and more stable configuration during low-activity states. We tried to determine the polarity of the global field of 18 Sco near activity minima by adding all available observations in each of the two minima covered as part of the spectropolarimetric monitoring. The noise reduction achieved through this strategy was not enough to provide us with field detection at activity minimum, however. A fourth detection in 2013, closer to the next activity maximum, supports an interpretation of negative polarities during this cycle period. In fact, positive definite detections from 2015 to 2019 seem to indicate that a second polarity reversal occurred sometime around the 2014 local maximum. Figure 3 shows the expected polarities when assuming reversals after each consecutive 7 yr cycle, in agreement with the observed data points.

3. Multicycle Period Search

The top panel of Figure 3 displays the resulting four-decade-long S-index composite time series after merging the calibrated and reduced data from seven different sources. Unfortunately, there is a 5 yr gap between 1985 and 1990, and because of this,
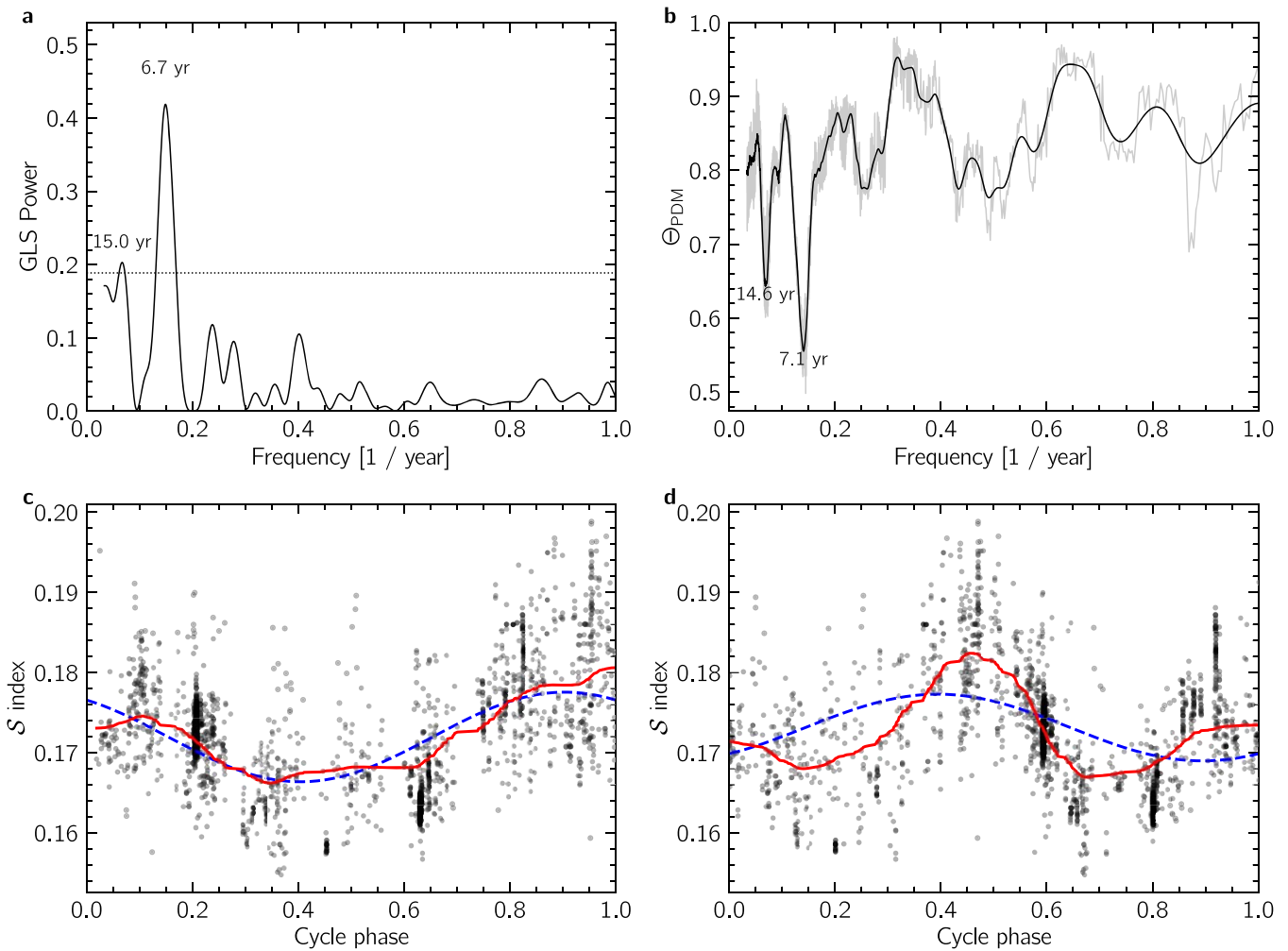
Figure 4. Global data analysis. (a) GLS periodogram. The dotted horizontal line indicates the level corresponding to a 10% false alarm probability. The corresponding periods of the two peaks above this level are annotated. (b) Θ statistic of PDM (lighter line) and its smoothed version (darker line). The corresponding periods of the two lowest minima are annotated. (c) Phase-folded data at 7.1 yr (primary PDM period). The dashed blue line is the sinusoidal GLS fit at this same frequency, and the red line is a moving average of the folded data. (d) Same as (c), but folded at 14.6 yr (secondary PDM period).

we discarded observations made prior to 1991 for the periodicity analysis. Nevertheless, they visually agree with the better-sampled subsequent data. The bottom panel of Figure 3 shows the remaining data, consisting of 31 yr, that we used for further analysis, together with a binned version of the data and a smooth spline interpolation, each representing a different level of processing used by different subsequent steps of our analysis.

To search for cycle components, we employed an ensemble of techniques. First, we searched for globally persistent cycle periods using the generalized Lomb–Scargle (GLS) period-ogram and the phase-dispersion minimization (PDM) algo-rithm. To ascertain the significance of the detected cycles, we used a hypothesis test that was centered around the model selection for a Gaussian process (GP) regression. Finally, we introduced a novel approach to identify time-varying cyclic behavior in the form of the Hilbert–Huang transform, a data-driven decomposition-based technique.

3.1. Global Data Analysis

In the foundational work of Baliunas et al. (1995) and Brandenburg et al. (1998), activity cycles were determined from chromospheric observations using the Lomb–Scargle

periodogram (Scargle 1982), arguably the most traditional and standard tool for finding persistent periodicities in unevenly sampled time-series data. Our first analysis of the 18 Sco data set was thus performed using the GLS periodogram (Zechme-ister & Kürster 2009), which also fits the mean offset and takes the uncertainties into account, and which is especially useful for composite observational data from different instruments. This was recently used by Boro Saikia et al. (2018b) to study the Mount Wilson sample.

Prior to this analysis, we first binned our data set to 80 day averages and estimated the bin variance using independent triangular windows, resulting in the blue squares shown in the bottom panel of Figure 3. This avoids biasing the fits toward the more densely sampled regions.

The resulting periodogram is shown in Figure 4(a). The power level corresponding to a false-alarm probability of 10% was computed using the bootstrap method and is shown as a horizontal line in the plot. Two clear peaks can be seen well above this level, the more prominent peak at 6.7 yr, and a secondary peak at 15.0 yr, which is at the detection limit. The peak widths are approximately constant in the frequency domain because they depend inversely on the observational baseline, and we used the half-width at half-maximum as an
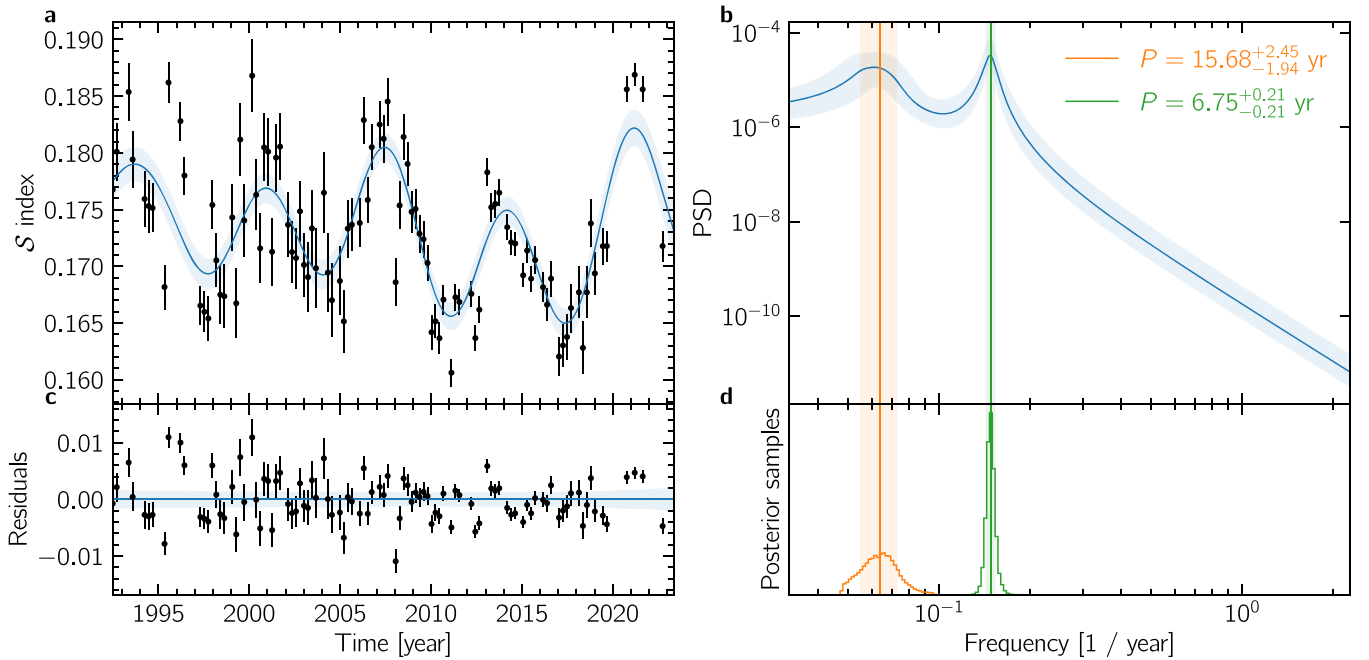
Figure 5. GP regression results based on a sum of two SHO terms (adopted solution). (a) Prediction of the maximum a posteriori model, with a shaded band between the 16th and 84th percentiles. (b) PSD of the process with uncertainties determined by an MCMC. The periods corresponding to the peaks are shown and highlighted. (c) Residuals after subtraction of the MAP predictions. (d) Samples of the oscillation frequency posterior probability distribution for each SHO, obtained via MCMC. The corresponding vertical bands encompass 68% of the posterior mass for these parameters.

Table 2
Comparison of Different GP Regression Models Based on Their Bayesian
Information Criteria and Leave-one-out Cross Validation

Models	ΔBIC	ΔLOO-CV
Reference Model:		
Single underdamped quasiperiodic SHO kernel	⋯	⋯
Tests for Additional Frequencies:		
Sum of two SHO terms	+2.8	+4.3
Sum of three SHO terms	−4.9	+7.0

Note. Based on these tests, we adopted the two-frequency model as our solution.

estimate of the uncertainty of each period. It is worth noting that the sampling window of the binned data, which is still not completely regular, also contributes to the overall structure of the periodogram, and this effect cannot be easily equalized (VanderPlas 2018).

For a more thorough analysis, we also considered another common global period-search method for unevenly sampled time series, the PDM (Stellingwerf 1978). The PDM consists of phase-folding the entire data set at many trial periods and computing the Θ statistic, which corresponds to the dispersion of the folded series.

The result of applying this method to our 18 Sco data is shown in Figure 4(b), with a smoothed version overlaid. This smoothing was used to better define the local minima. Analogously to the GLS, we highlight the two deepest minima, which are clearly separated from the others. The 7.1 and 14.6 yr periods appear to be consistent with the values recovered by the periodogram. We similarly used the half-width of the dips as a measure of the uncertainty for the reported periods.

Figures 4(c) and (d) show the folded time series as a function of the cycle phase for the 7.1 yr and 14.6 yr periods,

respectively. The sinusoidal fit of the GLS at these frequencies are also shown, together with a simple moving average. For the shorter period, the sine waveform agrees well with the actual shape of the cycle, with some deviations at the maximum, where the observations are sharper, and at minimum, where they are flatter, which is consistent with what is known about the solar cycle (Egeland et al. 2017) and what has been found from photometric observations of other stars (Reinhold et al. 2017). For the longer period, the W shape is indicative of the superposition of two cycles, with a more prominent maxima occurring when they are in phase.

3.2. Gaussian Process Regression and Model Selection

The methods used in the previous section, although useful, provide only an incomplete description that assumes harmonicities or strict periodicities in the magnetic activity variations. To take the nonlinearities of stellar activity cycles into account, a slightly more complex model is required. In this section, we perform GP regression with a quasiperiodic covariance function, in a similar fashion to what was proposed by Olpsert et al. (2018) in the context of the extended Mount Wilson sample.

More specifically, we consider covariance functions composed of a mixture of stochastically driven damped simple harmonic oscillators (SHOs; Foreman-Mackey et al. 2017). An SHO kernel is defined as

$$k_{\text{SHO}}(\tau) = S_0 \omega_0 Q \exp\left(-\frac{\omega_0 \tau}{2Q}\right), \qquad (7)$$

$$\left(\cos(\eta \omega_0 \tau) + \frac{1}{2\eta Q} \sin(\eta \omega_0 \tau)\right), \qquad (8)$$

where τ is the lag between two given time coordinates, ω_0 is the frequency of the undamped oscillator, Q is its quality factor, S_0
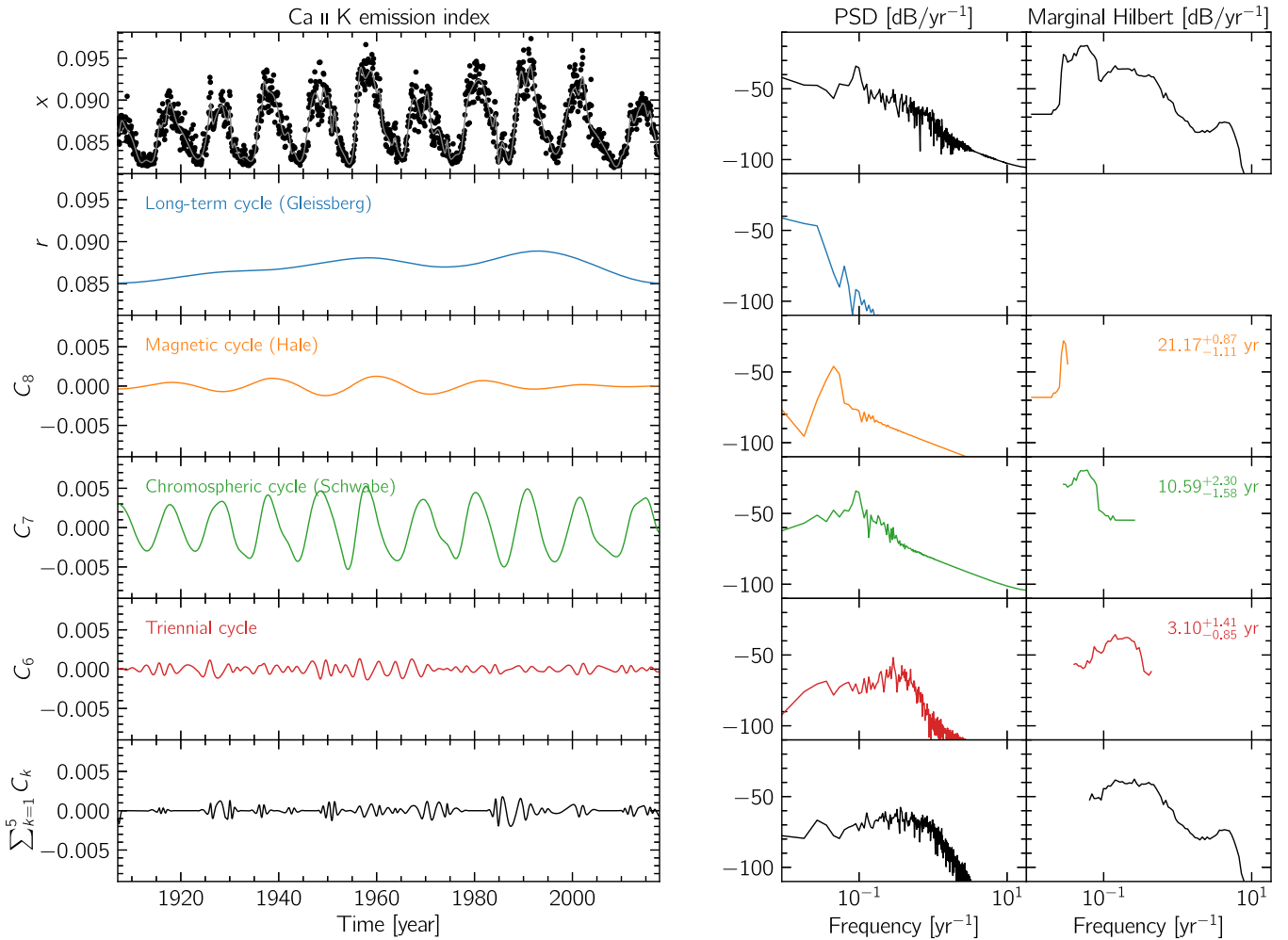
Figure 6. Decomposition of the solar K-line emission index. Left panels—time-domain representation for the original signal x, its trend component r, the identified cyclic components C_k, and the remaining high-frequency low-amplitude noise. Right panels—corresponding Fourier and Hilbert power spectral densities for each signal. The marginal Hilbert spectrum is used to estimate the frequency distribution of each cyclic component.

is proportional to the power spectral density (PSD) at $\omega = \omega_0$, and $\eta = \sqrt{1 - 1/(4Q^2)}$ describes the effect of damping on the characteristic oscillation frequency. When Q is large enough, $\eta \approx 1$.

To test the hypothesis that the data generating distribution consist of more than one quasiperiodic process, we performed model selection and hyperparameter optimization for families of covariance functions with one (reference model), two, and three SHO terms, using our binned data set for computational efficiency and filtering of higher-frequency phenomena (e.g., stellar rotation). For each case, we optimized the marginal likelihood using the limited-memory Broyden–Fletcher–Gold-farb–Shanno algorithm with bound constraints (L-BFGS-B; Byrd et al. 1995), and we repeated this optimization 10 different times with different random initializations to avoid becoming stuck in local maxima. The maximum a posteriori (MAP) model for each model family was then used to compute the Bayesian information criterion (BIC; Schwarz 1978) as well as the leave-one-out cross validation (LOO-CV; Rasmus-sen & Williams 2006). Table 2 provides a comparison of the multicomponent models with the reference model. Although both two and three frequencies result in a better generalization than one single kernel (higher LOO-CV), the increase in complexity captured by the BIC disfavors the three-oscillator

hypothesis. These tests indicate that the two-frequency model is indeed the best solution.

Having adopted the two SHO terms model, we sample the joint posterior probability of its hyperparameters using a Markov Chain Monte Carlo (MCMC) method, as in Foreman-Mackey et al. (2017). We run 24 chains for 20,000 steps and discard the first half as burn-in. Our results are presented in Figure 5. Figures 5(a) and (c) show the MAP prediction and its residuals, respectively. The samples of the posterior distribution for the inferred PSD and the two corresponding oscillator frequencies are plotted in Figures 5(b) and (d), respectively, with vertical bands encompassing the interval with 68% of posterior mass. These intervals are used as estimates for the two reported cycle periods and their associated uncertainties.

3.3. Time-series Decomposition Methods and Applications to the Solar Cycles

As shown by Oláh et al. (2016), time–frequency analysis can be used to reveal multiple and changing cycles in the Mount Wilson survey data set. In this section, we propose to extend this idea by using fully adaptive time–frequency methods with the specific purpose of disentangling multiple physically meaningful components from the data. The method described
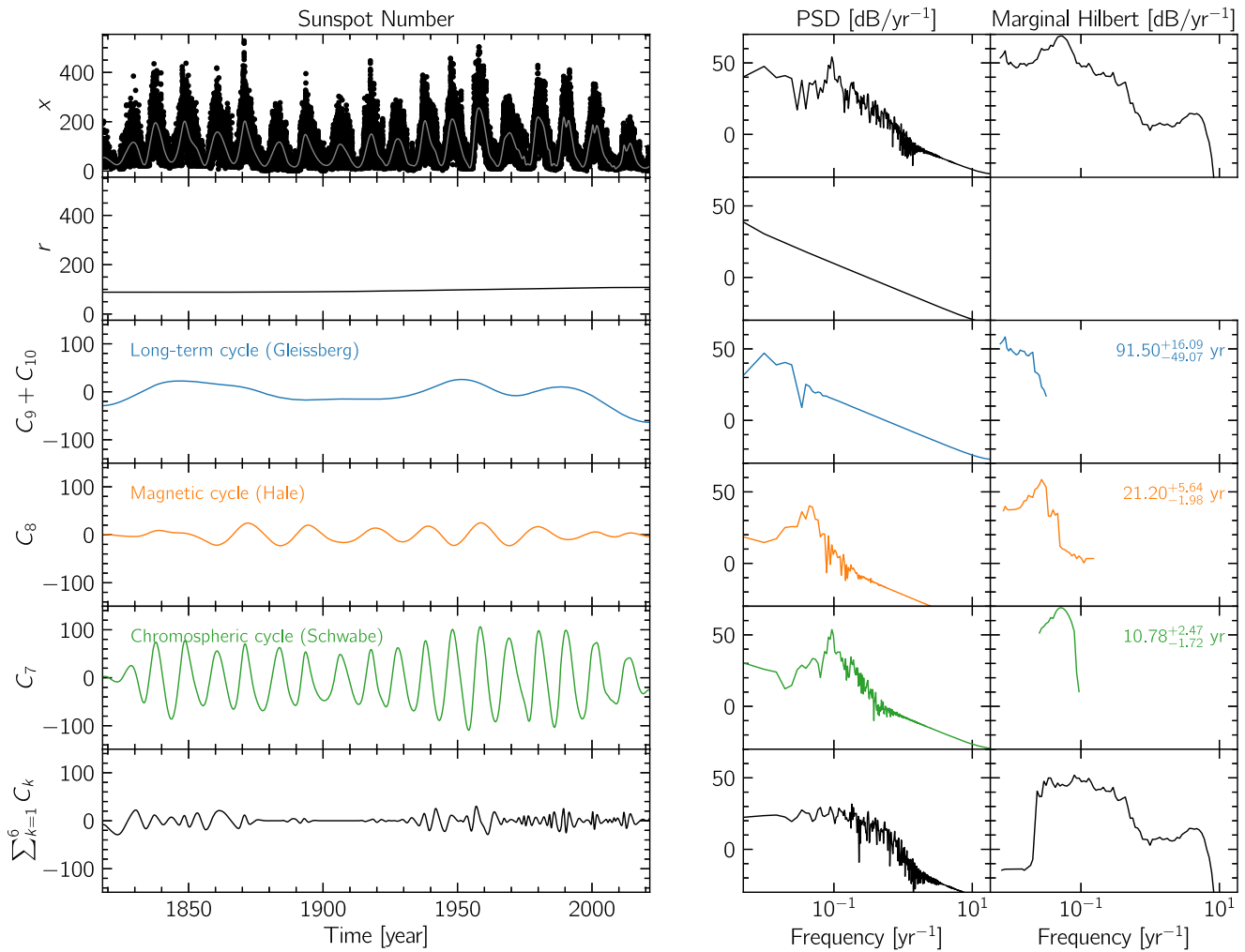
Figure 7. Same as Figure 6, but for the sunspot number time series.

here was originally developed and demonstrated by the authors in Velloso et al. (2023).

The Hilbert–Huang transform (HHT), based on the empirical mode decomposition (EMD; Huang et al. 1998), is a data-driven technique that addresses this exact issue. The goal of the Hilbert–Huang analysis is to decompose a signal into a sum of a finite number N of amplitude-modulated frequency-modulated (AM-FM) oscillations $C_k(t)$ ($k = 1, 2,...,N$) and some monotonic residue $r(t)$,

$$x(t) = \sum_{k=1}^{N} C_k(t) + r(t). \qquad (9)$$

These oscillations, known as intrinsic mode functions, present well-defined instantaneous values of amplitude and frequency. These can be derived from their analytic signal using the Hilbert transform. Many improvements to the original EMD algorithm have been proposed to address different issues arising from the original formulation. In this paper, we use a combination of the complete ensemble EMD with adaptive noise (Colominas et al. 2014) and the post-processing steps proposed in Wu & Huang (2009). The instantaneous frequency is then calculated on the resulting modes using the normalized Hilbert transform (Huang et al. 2009). Following a similar approach to the one used by Kolláth & Oláh (2009), we upsample the binned data to equally spaced 10-day steps with a cubic smoothing spline prior to our analysis. For 18 Sco, this is the solid line shown in the bottom panel of Figure 3.

The Hilbert–Huang analysis has been able to extract and characterize periodicities in solar cycles from many activity indicators, such as the sunspot number (Barnhart & Eichinger 2011; Gao 2017), the 10.7 cm radio flux, and helioseismic frequency shifts (Kolotkov et al. 2015). We tested the extent of our ability to recover multiple cycles on solar data using two different observational proxies: the daily total sunspot number series from 1818 to 2021 taken from the World Data Center SILSO,[11] and the composite K-line emission index from 1907 to 2017 (Bertello et al. 2016; Egeland et al. 2017).

The decomposition of the solar K-index is shown in Figure 6, revealing the well-known $\approx$11 yr Schwabe cycle, the shorter quasi-triennial cycle, and even the effect of the $\approx$22 yr Gnevyshev–Ohl rule, probably related to the Hale cycle. A long-term trend is captured by the residue of the decomposition, likely related to the Gleissberg cycle. Indeed, as seen in the decomposition of the sunspot number time series in Figure 7, the longer baseline enables us to resolve the long-term Gleissberg cycle, which presents the same overall shape in the last $\approx$100 yr as the trend found in the K-index. We note that in both cases, the Gleissberg cycle appears to modulate the
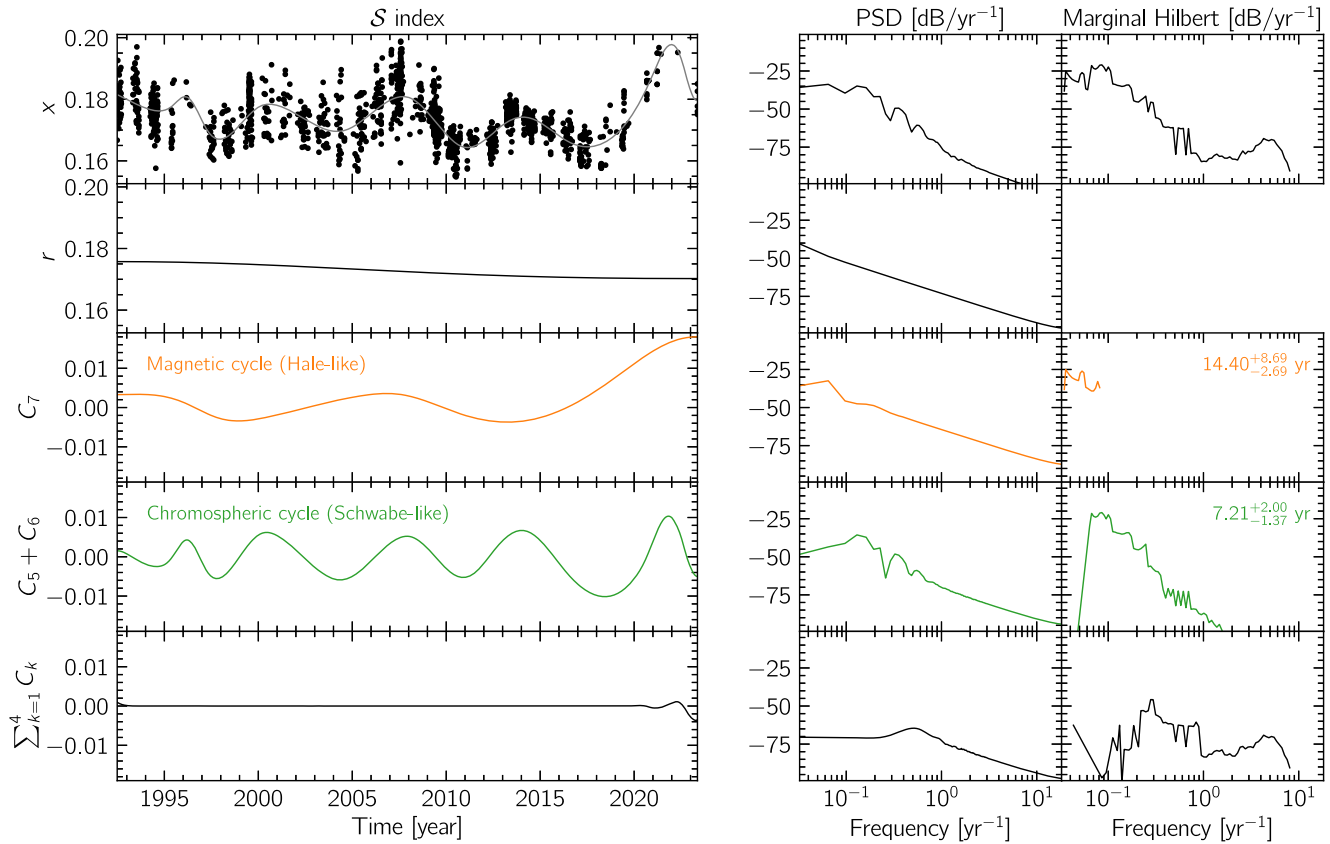
---

[11] https://www.sidc.be/silso/datafiles

Figure 8. Same as Figure 6, but for 18 Sco.

Table 3
Results from the Cycle Period Search

Method	P_{cyc}^1 (yr)	P_{cyc}^2 (yr)
Lomb–Scargle periodogram	6.71 ± 0.81	14.98 ± 4.35
Phase-dispersion minimization	7.12 ± 1.05	14.60 ± 3.66
Gaussian process regression	$6.75_{-0.21}^{+0.21}$	$15.68_{-1.94}^{+2.45}$
Hilbert–Huang transform	$7.21_{-1.37}^{+2.00}$	$14.40_{-2.69}^{+8.69}$
Average	6.95 ± 0.60	14.91 ± 2.67

amplitude of the chromospheric cycle, as expected, and the amplitude of the magnetic cycle is more stable.

Figure 8 presents the results of the same analysis for 18 Sco. In close agreement with the previous analyses, two oscillations are clearly defined: a higher-amplitude oscillation at ≈7 yr, and a longer oscillation at close to twice that period. This behavior seen in 18 Sco appears to be more active every other cycle and is reminiscent of what is seen in the Sun with the Gnevyshev–Ohl rule. Many studies have pointed out the relationship of this rule with the solar Hale cycle, although the reason is still not entirely clear, and it is reassuring to detect a similar modulation in a solar twin.

4. How Old is 18 Sco?

Over 40 studies based on model fitting (isochrones, activity, abundances, and rotation) present the age of 18 Sco as in the range of 2–6 Gyr, and only one study shows the age of 18 Sco as above 8 Gyr (Boyajian et al. 2012) and is considered an outlier by Sahlholdt et al. (2019). The most recent model-fitting ages are based on very precise stellar fundamental parameters

from differential spectroscopic analyses of Sahlholdt et al. (2019), and references therein. In these studies, the age is in the range 3–5 Gyr. The one age based on asteroseismology is slightly below 4 Gyr, which is consistent with all the model fits. The ages based on both gyrochronology and chromochronology agree well with all the model-fitting determinations. In this work, we used the most recent model-fitting ages of this star, as well as the age estimates from asteroseismology and gyrochronology. We give the age as 3.36–3.66 Gyr.

5. Results and Discussion

Table 3 summarizes the reported values for the two cycle periods found by each method in our ensemble, together with their uncertainties and a final average. We thus confirm the 6.95 ± 0.60 yr primary cycle for 18 Sco, while also suggesting a longer 14.91 ± 2.67 yr secondary cycle. Note that both the long and short cycles can be recognized by the eye in Figure 3, with the maximum activity level attained in approximately 1993.5, 2007.5, and 2021.5. Secondary maxima at intermediate epochs can also be observed.

Determining the secondary cycle in the manner presented in this paper with any reasonable confidence level was only possible because of our new measurements of the recent activity maximum with OPD, completing a continuous coverage of just over two magnetic cycles when combined with archival data. Continuing Lowell observations from 2011 (at minimum) to 2014 (at local maximum) had already hinted at an 18 Sco cycle longer (Brandenburg et al. 2017) than the ∼6.9 yr cycle (Hall et al. 2007) based on just over 7 yr of observations. The chromospheric activity displayed in Figure 3 also shows a

Table 4
Stellar Sample Properties

N	HD/KIC	Sp	$B-V$[a]	T_{eff}[a]	[Fe/H][a]	$\log\langle R'_{\text{HK}}\rangle$[a]	Age[a]	τ[a]	P_{rot}[a]	P^1_{cyc}[a]	P^2_{cyc}[a]	Ro
1	Sun	G2	0.66	5778	0.00	−4.90	4.6	12.6	25.4 ± 1.0	11.0 ± 2.0	22	2.0
2	1835	G3	0.66	5688	−0.02	−4.43	0.5	12.6	7.8 ± 0.6	...	9.1 ± 0.3	0.6
3	3651[b]	K0	0.84	5128	0.19	−4.99	7.2	20.6	44.0	13.8 ± 0.4	...	2.1
4	4628	K2	0.89	5035	−0.17	−4.85	5.3	21.7	38.5 ± 2.1	8.6 ± 0.1	...	1.8
5	10476[b]	K1	0.84	5188	−0.04	−4.91	4.9	20.6	35.2 ± 1.6	9.6 ± 0.1	...	1.7
6	16160	K3	0.98	4819	0.08	−4.96	6.9	22.8	48.0 ± 4.7	13.2 ± 0.2	...	2.1
7	17051	F8	0.57	6053	0.00	−4.60	0.6	7.5	8.5 ± 0.1	1.6	...	1.1
8	20630[b]	G5	0.66	5701	0.00	−4.42	0.7	12.6	9.2 ± 0.3	3.1 ± 0.01[c]	5.6 ± 0.1	0.7
9	22049[b]	K2	0.88	5152	0.00	−4.46	0.6	21.5	11.1 ± 0.1	2.9 ± 0.1	12.7 ± 0.3	0.5
10	26965	K1	0.82	5284	−0.04	−4.87	7.2	20.1	43.0	10.1 ± 0.1	...	2.1
11	30495	G1	0.63	5780	−0.08	−4.49	1.1	10.9	11.4 ± 0.2	1.7 ± 0.3	12.2 ± 3.0	1.0
12	32147	K5	1.06	4745	0.19	−4.95	6.3	23.5	48.0	11.1 ± 0.2	...	2.0
13	76151[b]	G3	0.67	5675	−0.04	−4.66	1.6	13.2	15.0	2.5 ± 0.1	...	1.1
14	78366[b]	G0	0.63	5915	−0.10	−4.61	0.8	10.9	9.7 ± 0.6	5.9 ± 0.1	12.2 ± 0.4	0.9
15	81809	K0	0.80	5623	−0.29	−4.92	6.6	19.4	40.2 ± 3.0	8.2 ± 0.1	...	2.1
16	114710	F9	0.58	5970	−0.06	−4.75	1.7	8.0	12.3 ± 1.1	9.6 ± 0.3	16.6 ± 0.6	1.5
17	115404	K1	0.93	5081	−0.16	−4.48	1.4	22.3	18.5 ± 1.3	...	12.4 ± 0.4	0.8
18	128620	G2	0.71	5809	0.23	−5.00	5.4	15.4	22.5 ± 5.9	19.2 ± 0.7	...	1.5
19	128621	K1	0.88	5230	0.27	−4.93	5.4	21.5	36.2 ± 1.4	8.1 ± 0.2	...	1.7
20	**146233[b]**	**G2**	**0.65**	**5767**	**−0.02**	**−4.93**	**4.1**	**12.0**	**22.7 ± 0.5**	**6.9[d]**	**14.9[d]**	**1.9**
21	149661	K2	0.80	5199	−0.01	−4.58	2.1	19.4	21.1 ± 1.4	4.0 ± 0.1	17.4 ± 0.7	1.1
22	152391	G7	0.76	5420	−0.08	−4.45	0.8	17.8	11.4 ± 1.4	...	10.9 ± 0.2	0.6
23	156026	K5	1.16	4600	−0.34	−4.66	1.3	24.2	21.0	...	21.0 ± 0.9	0.9
24	160346	K3	0.96	4797	−0.09	−4.79	4.4	22.7	36.4 ± 1.2	7.0 ± 0.1	...	1.6
25	165341A	K1	0.78	5023	−0.29	−4.55	2.0	18.6	19.9	5.1 ± 0.1	15.5	1.1
26	166620	K5	0.90	5000	−0.08	−4.96	6.2	21.9	42.4 ± 3.7	15.8 ± 0.3	...	1.9
27	190406	G1	0.61	5847	−0.12	−4.80	1.8	9.7	13.9 ± 1.5	2.6 ± 0.1	16.9 ± 0.8	1.4
28	201091[b]	K5	1.18	4400	−0.20	−4.76	3.3	24.4	35.4 ± 9.2	7.3 ± 0.1	...	1.5
29	201092	K7	1.37	4040	−0.27	−4.89	3.2	25.9	37.8 ± 7.4	11.7 ± 0.4	...	1.5
30	219834B	K2	0.91	5136	0.24	−4.94	6.2	22.1	43.0	10.0 ± 0.2	...	1.9
31	100180	F7	0.57	5942	−0.15	−4.92	2.3	7.5	14.0	3.6 ± 0.1	12.9 ± 0.5	1.9
32	103095	K1	0.75	5035	−1.36	−4.90	4.6	17.4	31.0	7.3 ± 0.1	...	1.8
33	173701	G8	0.84	5488	0.34	−5.00	4.6	20.6	29.8 ± 3.1	7.4 ± 1.2	...	1.4
34	10644253	G0	0.59	6045	0.06	−4.69	0.9	8.6	10.9 ± 0.9	1.5 ± 0.1	...	1.3

Notes. The bold values emphasize the row for the main target of this paper (18 Scorpii).
[a] From Brandenburg et al. (2017).
[b] Stars with ZDI measurements in the literature.
[c] From Boro Saikia et al. (2022).
[d] Measured cycles from this study for HD 78366 (14), HD 128620 (18), and 18 Sco (20).

regular decrease between 2000 and 2004, followed by a sharp growth between 2004 and 2007.

Another piece of evidence supporting the detected behavior is provided by stellar spectropolarimetric observations from NARVAL, extending from 2007 up to 2019 (Figure 3). Measurements recorded in the summer of 2007 are likely to be representative of a high-activity state. At this time, a magnetic field density stronger than 3.5 Gauss (Petit et al. 2008) was detected, and was reconstructed as a predominantly quadrupolar field (56% of the poloidal magnetic energy). This predominantly quadrupolar magnetic geometry at that time is consistent with the magnetic topology of the Sun at solar maximum. However, one cycle period later, in 2014, when a local maximum in the S-index occurred, NARVAL starts to detect a slightly less intense magnetic field with the opposite polarity. These observations all support our hypothesis that 18 Sco, like the Sun, changes its magnetic topology and flips polarity after each consecutive cycle, generating a Hale-like effect in the observed activity.

The consequences of this result can be better appreciated by situating 18 Sco within the context of other stars with two

or more measured cycles in the literature. Table 4 presents a sample of these stars and their respective properties, compiled from Brandenburg et al. (2017) and Boro Saikia et al. (2022). For the G-type star HD 78366 (number 14 in Table 4) and for the F-type star HD 114710 (number 16), we also found a set of hitherto unpublished short cycles of 1.42 and 1.74 yr, respectively, using the same method (see Appendix A). Figure 9 shows the P_{cyc} measurements for 18 Sco in this wider stellar context, including the Sun. Prior work has described the relationship between rotation and cycle periods as elucidating two distinct branches in these P_{cyc}–P_{rot} diagrams, called "active" and "inactive" (Noyes et al. 1984; Böhm-Vitense 2007). The position of the Sun between these branches has accordingly been used to support the hypothesis of a possible transition between the branches (Metcalfe et al. 2022). Studies have also postulated a third branch that shows an anticorrelation between cycle period and rotation period for faster spinners (Saar & Brandenburg 1999; Lehtinen et al. 2016). However, subsequent observations stretching over the last decade for solar-type stars suggest a more nuanced interpretation of this diagram, where
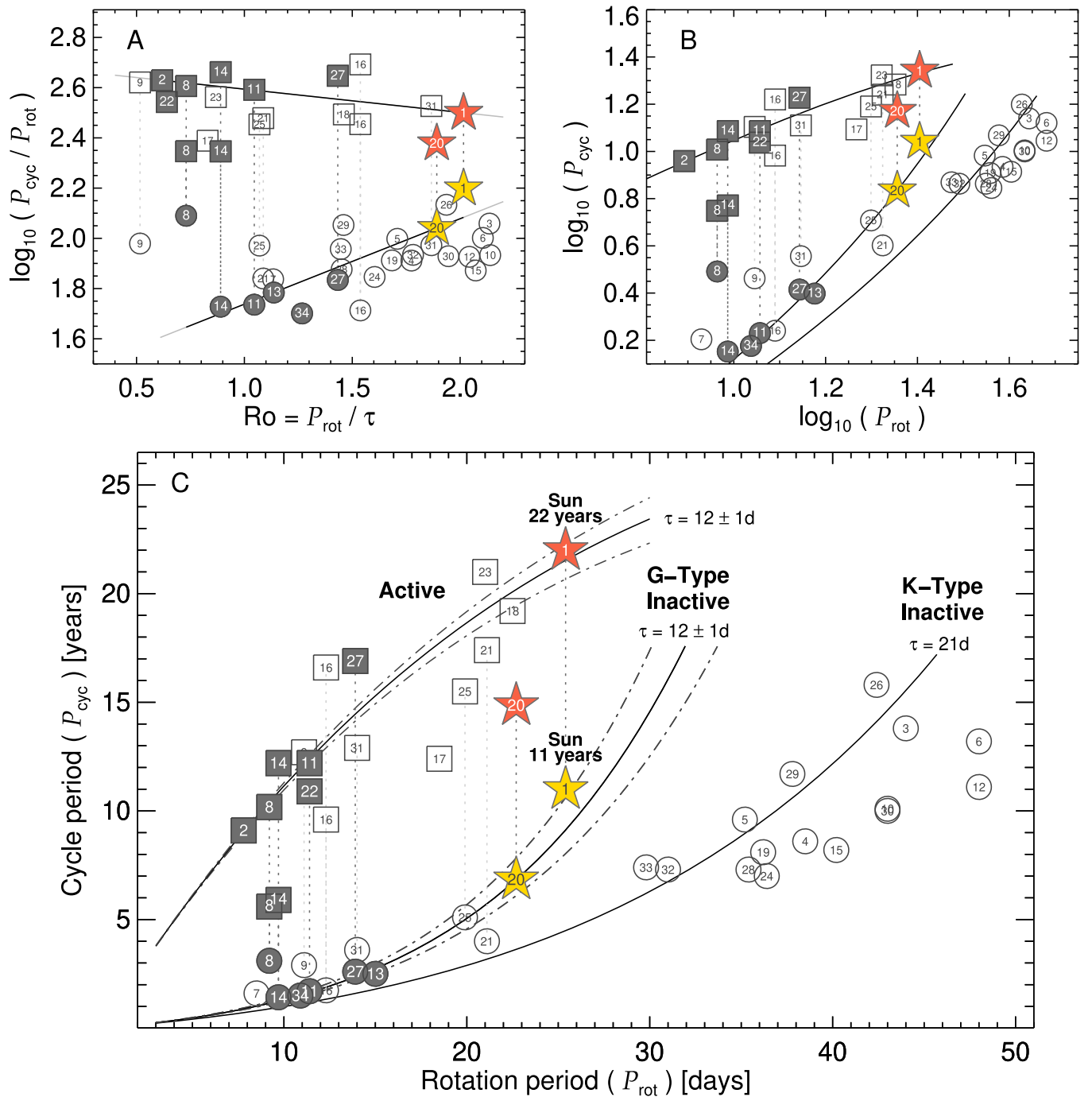
Figure 9. Three representations of the relationship between cycle duration and rotation period (A). Fits from Equation (10) as a function of Ro. (B) Same fits for a fixed value of $\tau = 12$ days and $\tau = 21$ days for the lower branch. (C) Same as panel (B), but on a linear scale. G-type stars are displayed with filled symbols, and F- and K-type stars are shown as open symbols. The circles represent stellar cycles that lie on the inactive branch, while the squares represent either the additional longer cycles for multicyclic stars or monocycle stars lying on the active branch. The Sun (1) and 18 Sco (20), both G-type stars, are indicated with colored stars, with the Schwabe-like component in yellow and the Hale-like component in red. Multiple cycles observed in the same star are connected with vertical dotted lines. Our proposed new fits are displayed with solid lines for two values of convective turnover times corresponding to G- and K-type stars, while the dashed–dotted lines represent the corresponding variance intervals from changing τ by ± 1 day. The data were compiled from Brandenburg et al. (2017) and Boro Saikia et al. (2022).

the existence of well-defined branches itself has been questioned (See et al. 2016; Strugarek et al. 2017; Boro Saikia et al. 2018b).

In this work, we fit $\log_{10}(P_{\mathrm{cyc}}/P_{\mathrm{rot}})$ as two linear branches with respect to the Rossby number $\mathrm{Ro} = P_{\mathrm{rot}}/\tau$, where τ is the convective turnover time, as shown in Figure 9(A). The linear fits were obtained by grouping the shortest periods of each star in the lower "inactive" branch and the longest in the upper

"active" branch, resulting in the following equations:

$$\log_{10}\left(\frac{P_{\mathrm{cyc}}}{P_{\mathrm{rot}}}\right) = \begin{cases} 0.340\dfrac{P_{\mathrm{rot}}}{\tau} + 1.398, & \text{``inactive''} \\[2mm] -0.093\dfrac{P_{\mathrm{rot}}}{\tau} + 2.686, & \text{``active''}. \end{cases} \quad (10)$$

Equation (10) yields a different cycle–rotation relationship for each fixed value of τ, meaning a family of tracks can be

defined in P_{cyc}–P_{rot} space for each branch, varying with spectral type. This transformation is shown on a logarithmic scale in Figure 9(B), in which two sample values of $\tau = 12$ days and $\tau = 21$ days were used in the lower branch to illustrate the separation observed between G-type and K-type stars, respectively. This same diagram is shown on a linear scale in Figure 9(C), in which the dependence on spectral type for the lower branch is clear. The variations with τ are significantly lower in the upper branch because the magnitude of the slope in the exponent is lower (weaker correlation in panel (C)).

Our results suggest that at least some stars that are commonly placed on the active branch of these diagrams are likely stars exhibiting Hale-like magnetic cycles with corresponding Schwabe-like (activity amplitude) cycles elsewhere, and $P_{cyc,Hale} \approx 2P_{cyc,Schwabe}$ (Figure 9). Some monocyclic stars in the diagram may have near-equal amplitude Schwabe and Hale cycles, and thus $P_{cyc,Schwabe}$ and $P_{cyc,Hale}$ are indistinguishable without detailed ZDI measurements. The detection of very short cycles in some stars (with $P_{cyc,long} \gg 2P_{cyc,short}$) does not necessarily contradict this: their modulations may originate in other phenomena that are not necessarily directly connected to cycles, analogously to the solar Rieger cycles, or they might be the result of magnetic Rossby waves (Zaqarashvili et al. 2015). Alternatively, the very short cycles may be due to a dynamo with a quite different origin and mechanism, which should perhaps properly be considered separately—for example, a surface shear layer dynamo (Brandenburg 2005; Brandenburg et al. 2017). Comprehending the multiple origins of stars in Figure 9 is an important step toward understanding the pattern of cycle periods in stars better, in particular, if there is a real physical meaning to the apparent branch structure, and which parameters control it.

6. Conclusion

The results presented here have wider implications for solar/stellar magnetism. While the solar proxy Kappa 1 Cet (∼0.7 Gyr; spectral type G5V) has illuminated the Sun–Earth relationship at the Archean eon (do Nascimento et al. 2016), 18 Sco, with its age of 3.4–3.7 Gyr and its ≈15 yr magnetic cycle, informs us that the cycles in the younger Sun during Earth's Precambrian era were shorter than they are today. Thus, we are beginning to build up an evolutionary sequence for solar-like cycles. If Sun-like stars commonly exhibit magnetic cycles similar to those of the Sun and 18 Sco, including topological changes such as the quadrupole-dipole flips seen in both, these magnetic geometry changes will be important for governing stellar winds and coronal mass ejection trajectories. These in turn have significance for angular momentum losses and interactions with any planets (Strugarek et al. 2015).

We also see from the 18 Sco S-index observations that when their amplitudes differ, it is possible to detect separate Schwabe (amplitude) and Hale (magnetic polarity) cycles in nonmagnetic data (e.g., activity modulation). Careful searches for these separate cycles in other stars ought to be undertaken; new ZDI data can be used to separate the hidden Hale cycles when Hale and Schwabe amplitudes are too similar. This Hale–Schwabe cycle twinning may be commonplace among stars, but may be somewhat hidden if the activity amplitudes are too similar. This is in fact expected in nonlinear dynamos at low magnetic Prandtl number (Brandenburg 2005; Zaqarashvili et al. 2015;

Weiss & Tobias 2016). Our sample is tiny here; larger, similarly detailed data sets for other solar-like stars with well-determined cycles are essential for a full understanding of the impact of fundamental parameters on the evolution of the dynamo. Further ZDI data specifically for 18 Sco will also be useful; we predict a return to a predominantly quadrupolar topology and an overall polarity reversal in 2022 (see Figure 1).

In conclusion, we found a distinct ≈15 yr cycle for 18 Sco, which is the best solar twin known to date, co-existent with the already published 6.9 yr cycle. The following observation seasons will more precisely confirm the duration of this cycle. This cycle in chromospheric HK activity seems to coincide with magnetic polarity changes, indicating that it is analogous to the 22 yr Hale magnetic cycle of the Sun, which then makes the shorter 6.9 yr cycle equivalent to the solar Schwabe (activity amplitude) cycle. 18 Sco would thus appear to have twinned magnetic and activity cycles quite similar to those of the Sun, with $P_{cyc,Hale} \approx 2P_{cyc,Schwabe}$, but with shorter periods, which might perhaps be due to its somewhat younger age. We suggest that there may be many such twinned Hale–Schwabe cycles (some hidden by equal amplitudes). Part of the reason for the scattered character of the active branch in P_{cyc}–P_{rot} (and similar) diagrams may be due to the scattering of these twins, plus the multiple disparate physical origins for many other real and apparent cycles often placed in these diagrams (some of which may not actually belong there). We encourage further analysis of existing time series and new and old ZDI data to search for more Hale–Schwabe cycle pairs.

Appendix A
Cycle Period Analysis for HD 78366 and HD 114710

As mentioned in Section 5, a side result of our method was the determination of as yet unpublished short cycles in the G-type star HD 78366 and in the F-type star HD 114710. This appendix provides the corresponding analysis in greater detail.

The same data-preprocessing steps were taken to ensure that the time series were compatible with the assumptions for each method. For both stars, we only had access to Mount Wilson
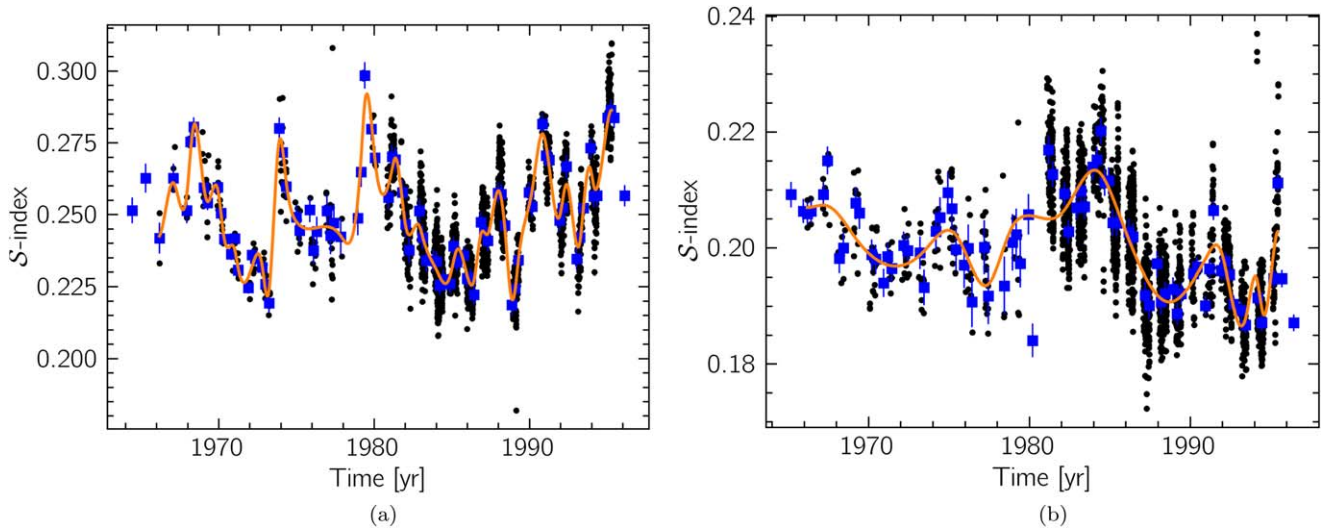
Figure 10. Preprocessed S-index time series taken from Mount Wilson Observatory observations from 1966 to 1995. Blue squares are seasonal averages used by the GLS periodogram and GP regression, and the orange line is a smooth spline interpolation used by the HHT. The panels show both stars: (a) HD 78366, and (b) HD 114710.
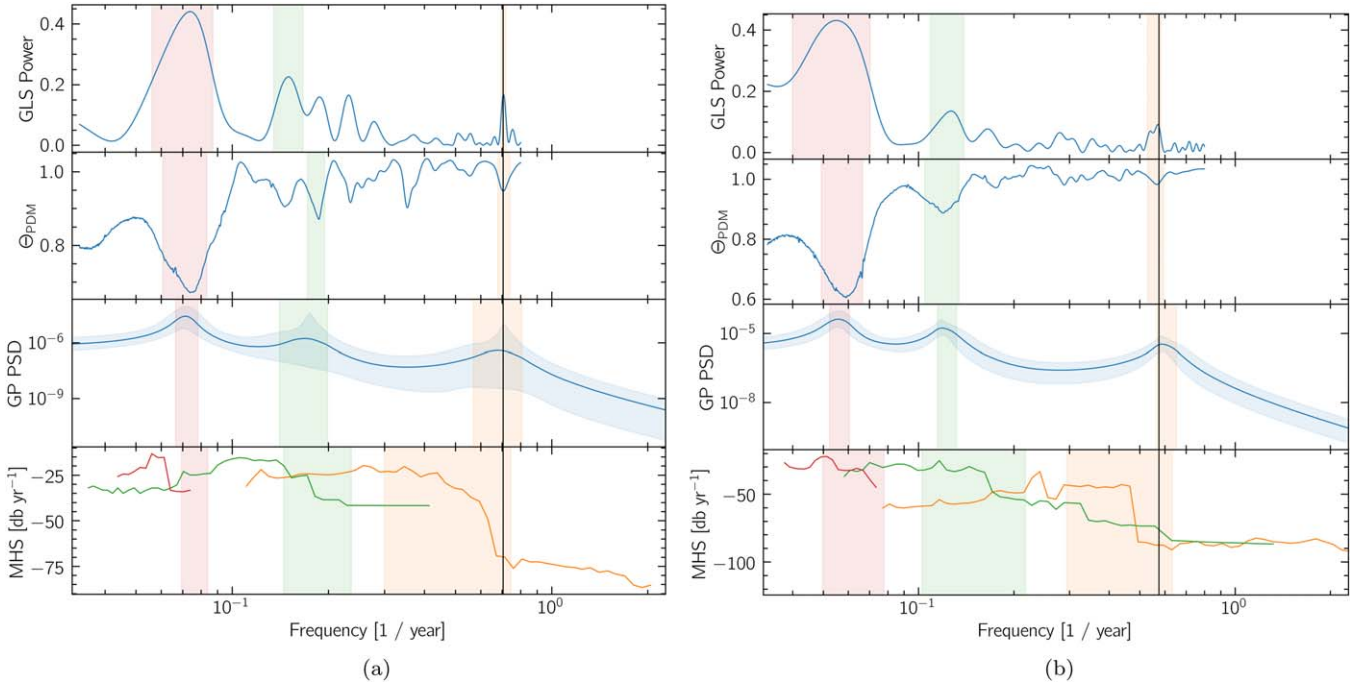

Figure 11. Summary of the results after applying our analysis to the S-index data of both stars. The panels show from top to bottom the GLS periodogram, the PDM statistic, the PSD obtained from MCMC sampling a triple-frequency GP model, and the marginal Hilbert spectrum. The colored strips in each panel indicate the confidence intervals for the three main periods found by each method. The vertical black line represents the newly determined third period: (a) 1.42 yr (HD 78366), and (b) 1.74 yr (HD 114710).

Observatory observations spanning almost 30 yr from 1966 up to 1995. Figure 10 illustrates the observations for both targets together with the preprocessed data sets, using the same representation as in Figure 3.

Figure 11 summarizes the result of applying our ensemble of four period-search methods to these data sets. In each case, we have tested for the assumption of a possible third frequency, which the HHT decomposition reveals and the GP regression appears to confirm. The two known longer periods for each case are recovered as expected, and the average values for the

third cycle are shown as a vertical black line at 1.42 yr for HD 78366 and at 1.74 yr for HD 114710.

We note that in contrast with the same analysis for 18 Sco, these shortest periods appear to be localized in time, similar to the rapid variations found in ξ Boo A, ϵ Eri, and HN Peg (Morgenthaler et al. 2012; Jeffers et al. 2014; Boro Saikia et al. 2015). This implies a less clear signature found by global analysis methods, especially by PDM. These periods are also close to the lower possible detection limit with the available binned ground-based data.

Appendix B
Spectropolarimetric Observations

This appendix presents the journal of spectropolarimetric observations from ESPaDOnS and NARVAL in Table 5 below.

Table 5
Journal of ESPaDOnS/NARVAL Observations

Julian Date (2 450 000+)	B_ℓ (G)	Mag. Detection	Airmass	Instrument	Signal-to-noise Ratio (Max)
3540.79918	-0.0 ± 0.7	No	1.273	ESPaDOnS	486
3541.77398	0.9 ± 0.6	No	1.39	ESPaDOnS	550
4128.74754	1.0 ± 0.3	MARGINAL	1.861	NARVAL	1017
4129.74760	0.5 ± 0.3	No	1.841	NARVAL	1101
4130.75273	-0.2 ± 0.3	No	1.6	NARVAL	1240
4133.76567	-0.3 ± 0.5	No	1.679	NARVAL	697
4134.75835	0.9 ± 0.3	No	1.707	NARVAL	1142
4135.76501	1.0 ± 0.4	No	1.667	NARVAL	901
4307.41343	-3.4 ± 0.5	DEFINITE	1.812	NARVAL	757
4309.36560	-1.7 ± 0.2	DEFINITE	1.637	NARVAL	1570
4311.38248	-0.2 ± 0.2	No	1.707	NARVAL	1666
4312.37051	0.8 ± 0.2	DEFINITE	1.673	NARVAL	1716
4313.37235	1.0 ± 0.3	No	1.69	NARVAL	1055
4315.37102	0.1 ± 0.2	No	1.707	NARVAL	1502
4316.37385	-0.2 ± 0.2	MARGINAL	1.732	NARVAL	1572
4317.36790	-0.7 ± 0.3	No	1.718	NARVAL	1269
4322.36678	0.6 ± 0.3	No	1.785	NARVAL	1253
4323.36959	0.8 ± 0.3	No	1.82	NARVAL	1114
4331.35463	-1.7 ± 0.2	DEFINITE	1.875	NARVAL	1440
4688.35813	-0.5 ± 0.2	No	1.748	NARVAL	1563
4697.34307	-1.5 ± 0.6	No	1.805	NARVAL	595
4699.33743	-0.1 ± 0.2	No	1.808	NARVAL	1455
4708.36384	-0.3 ± 0.3	No	2.392	NARVAL	1320
4984.57743	0.6 ± 0.3	No	1.925	NARVAL	1321
4985.49497	0.3 ± 0.2	No	1.607	NARVAL	1560
4986.50292	0.1 ± 0.2	No	1.616	NARVAL	1547
4994.53008	-0.1 ± 0.3	No	1.782	NARVAL	1104
4995.49106	0.7 ± 0.4	No	1.639	NARVAL	904
5001.47260	-0.3 ± 1.0	No	1.85	NARVAL	841
5001.52117	-0.0 ± 0.5	No	1.635	NARVAL	589
5005.54228	0.8 ± 0.3	No	2.18	NARVAL	1182
5006.52697	0.4 ± 0.3	No	2.019	NARVAL	1274
5007.52348	-0.1 ± 0.3	No	2.024	NARVAL	1246
5010.42424	-0.6 ± 0.3	No	1.607	NARVAL	1054
5011.40999	-0.1 ± 0.3	No	1.609	NARVAL	1047
5013.51035	-0.6 ± 0.3	No	2.058	NARVAL	1196
5017.41789	0.0 ± 0.8	No	1.618	NARVAL	945
5018.42796	-0.0 ± 0.2	No	1.641	NARVAL	1551
5202.74088	0.8 ± 0.3	No	2.951	NARVAL	1101
5219.70649	-2.8 ± 0.9	No	2.651	NARVAL	450
5354.44915	-0.5 ± 0.3	No	1.641	NARVAL	1369
5370.48571	0.3 ± 0.3	No	1.709	NARVAL	1294
5379.43961	-0.1 ± 0.3	No	1.641	NARVAL	1373
5382.45079	-0.1 ± 0.2	No	1.703	NARVAL	1483
5384.42995	-0.1 ± 0.2	No	1.651	NARVAL	1769
5388.42838	0.1 ± 0.2	No	1.681	NARVAL	1518
5392.44455	0.2 ± 0.3	No	1.812	NARVAL	1396
5402.41754	-0.4 ± 0.2	No	1.825	NARVAL	1442
5403.43567	-0.4 ± 0.2	No	2.001	NARVAL	1507
5412.39604	0.1 ± 0.2	No	1.874	NARVAL	1485
6161.35456	0.3 ± 0.3	No	1.967	NARVAL	1383
6162.34410	0.0 ± 0.3	No	1.897	NARVAL	1081
6407.66111	-1.4 ± 0.2	DEFINITE	1.78	NARVAL	1492
6448.50228	0.6 ± 0.3	No	1.619	NARVAL	1333
6454.48395	-1.0 ± 0.3	No	1.617	NARVAL	1119
6459.45896	-0.3 ± 0.3	No	1.608	NARVAL	1284

15

Table 5

(Continued)

Julian Date (2 450 000+)	B_ℓ (G)	Mag. Detection	Airmass	Instrument	Signal-to-noise Ratio (Max)
6473.47494	-0.3 ± 0.3	MARGINAL	1.754	NARVAL	1341
6480.45608	-0.9 ± 0.2	MARGINAL	1.757	NARVAL	1633
6485.45449	0.4 ± 0.3	No	1.833	NARVAL	1272
7126.55351	1.4 ± 0.3	DEFINITE	1.83	NARVAL	1432
7142.60446	0.1 ± 0.2	No	1.624	NARVAL	1578
7568.44611	1.1 ± 0.3	DEFINITE	1.64	NARVAL	1384
7576.54823	-0.4 ± 0.4	No	3.307	NARVAL	1196
7606.36967	0.7 ± 0.2	DEFINITE	1.75	NARVAL	1528
7911.43234	0.4 ± 0.2	No	1.691	NARVAL	1560
7939.40837	-0.5 ± 0.3	No	1.609	NARVAL	1449
8294.43873	-0.1 ± 0.3	No	1.61	NARVAL	1404
8322.42160	0.5 ± 0.3	MARGINAL	1.815	NARVAL	1541
8646.44874	-0.5 ± 0.4	No	1.619	NARVAL	1008
8653.39759	1.6 ± 0.4	DEFINITE	1.703	NARVAL	950

ORCID iDs

J.-D. do Nascimento, Jr. ⓘ https://orcid.org/0000-0001-7804-2145
S. A. Barnes ⓘ https://orcid.org/0000-0001-7152-5726
S. H. Saar ⓘ https://orcid.org/0000-0001-7032-8480
G. F. Porto de Mello ⓘ https://orcid.org/0000-0003-0911-1324
F. Anthony ⓘ https://orcid.org/0000-0003-1963-636X
L. de Almeida ⓘ https://orcid.org/0000-0001-8179-1147
E. N. Velloso ⓘ https://orcid.org/0000-0002-9668-5547
J. S. da Costa ⓘ https://orcid.org/0000-0002-9830-0495
P. Petit ⓘ https://orcid.org/0000-0001-7624-9222
A. Strugarek ⓘ https://orcid.org/0000-0002-9630-6463
B. J. Wargelin ⓘ https://orcid.org/0000-0002-2096-9586
M. Castro ⓘ https://orcid.org/0000-0002-1332-2477
K. G. Strassmeier ⓘ https://orcid.org/0000-0002-6192-6494
A. S. Brun ⓘ https://orcid.org/0000-0002-1729-8267

References

Astropy Collaboration, Robitaille, T. P., Tollerud, E. J., et al. 2013, A&A, 558, A33
Aurière, M. 2003, in EAS Publications Ser. 9, Magnetism and Activity of the Sun and Stars, ed. J. Arnaud & N. Meunier (Les Ulis: EDP Sciences), 105
Babcock, H. W. 1961, ApJ, 133, 572
Baliunas, S. L., Donahue, R. A., Soon, W. H., et al. 1995, ApJ, 438, 269
Barnhart, B. L., & Eichinger, W. E. 2011, SoPh, 269, 439
Bazot, M., Campante, T. L., Chaplin, W. J., et al. 2012, A&A, 544, A106
Bazot, M., Creevey, O., Christensen-Dalsgaard, J., & Meléndez, J. 2018, A&A, 619, A172
Bazot, M., Ireland, M. J., Huber, D., et al. 2011, A&A, 526, L4
Bertello, L., Pevtsov, A., Tlatov, A., & Singh, J. 2016, SoPh, 291, 2967
Böhm-Vitense, E. 2007, ApJ, 657, 486
Bonanno, A., Schlattl, H., & Paternò, L. 2002, A&A, 390, 1115
Boro Saikia, S., Jeffers, S. V., Morin, J., et al. 2016, A&A, 594, A29
Boro Saikia, S., Jeffers, S. V., Petit, P., et al. 2015, A&A, 573, A17
Boro Saikia, S., Lueftinger, T., Jeffers, S. V., et al. 2018a, A&A, 620, L11
Boro Saikia, S., Lüftinger, T., Folsom, C. P., et al. 2022, A&A, 658, A16
Boro Saikia, S., Marvin, C. J., Jeffers, S. V., et al. 2018b, A&A, 616, A108
Bouchy, F. & Sophie Team 2006, in Coll. OHP: Tenth Anniversary of 51 Peg-b: Status of and Prospects for Hot Jupiter Studies, ed. L. Arnold, F. Bouchy, & C. Moutou (Paris: Frontier Group), 319
Boyajian, T. S., McAlister, H. A., van Belle, G., et al. 2012, ApJ, 746, 101
Brandenburg, A. 2005, ApJ, 625, 539
Brandenburg, A., Mathur, S., & Metcalfe, T. S. 2017, ApJ, 845, 79
Brandenburg, A., Saar, S. H., & Turpin, C. R. 1998, ApJL, 498, L51
Brun, A. S., & Browning, M. K. 2017, LRSP, 14, 4
Brun, A. S., Strugarek, A., Noraz, Q., et al. 2022, ApJ, 926, 21
Byrd, R. H., Lu, P., Nocedal, J., & Zhu, C. 1995, SJSC, 16, 1190
Cayrel de Strobel, G. 1996, A&ARv, 7, 243
Charbonneau, P. 2010, LRSP, 7, 3
Colominas, M. A., Schlotthauer, G., & Torres, M. E. 2014, Biomedical Signal Processing and Control, 14, 19
Datson, J., Flynn, C., & Portinari, L. 2012, MNRAS, 426, 484
Datson, J., Flynn, C., & Portinari, L. 2014, MNRAS, 439, 1028
Dikpati, M., de Toma, G., Gilman, P. A., Arge, C. N., & White, O. R. 2004, ApJ, 601, 1136
do Nascimento, J. D., Vidotto, A. A., Petit, P., et al. 2016, ApJL, 820, L15
Donati, J. F., Semel, M., Carter, B. D., Rees, D. E., & Collier Cameron, A. 1997, MNRAS, 291, 658
Duncan, D. K., Vaughan, A. H., Wilson, O. C., et al. 1991, ApJS, 76, 383
Egeland, R., Soon, W., Baliunas, S., et al. 2017, ApJ, 835, 25
Foreman-Mackey, D., Agol, E., Ambikasaran, S., & Angus, R. 2017, AJ, 154, 220
Foreman-Mackey, D., Hogg, D. W., Lang, D., & Goodman, J. 2013, PASP, 125, 306
Gao, P. X. 2017, MNRAS, 472, 2913
Hale, G. E., Ellerman, F., Nicholson, S. B., & Joy, A. H. 1919, ApJ, 49, 153
Hall, J. C., Henry, G. W., & Lockwood, G. W. 2007, AJ, 133, 2206
Hardorp, J. 1978, A&A, 63, 383
Harris, C. R., Millman, K. J., van der Walt, S. J., et al. 2020, Natur, 585, 357
Hathaway, D. H. 2015, LRSP, 12, 4
Huang, N. E., Shen, Z., Long, S. R., et al. 1998, RSPSA, 454, 903
Huang, N. E., Wu, Z., Long, S. R., et al. 2009, Advances in Adaptive Data Analysis, 01, 177
Hunter, J. D. 2007, CSE, 9, 90
Jeffers, S. V., Petit, P., Marsden, S. C., et al. 2014, A&A, 569, A79
Kochukhov, O., Makaganiuk, V., & Piskunov, N. 2010, A&A, 524, A5
Kolláth, Z., & Oláh, K. 2009, A&A, 501, 695
Kolotkov, D. Y., Broomhall, A. M., & Nakariakov, V. M. 2015, MNRAS, 451, 4360
Lehtinen, J., Jetsu, L., Hackman, T., Kajatkari, P., & Henry, G. W. 2016, A&A, 588, A38
Leighton, R. B. 1969, ApJ, 156, 1
Li, T. D., Bi, S. L., Liu, K., Tian, Z. J., & Shuai, G. Z. 2012, A&A, 546, A83
Luck, R. E., & Heiter, U. 2005, AJ, 129, 1063
Mamajek, E. E., Prsa, A., Torres, G., et al. 2015, arXiv:1510.07674
Mayor, M., Pepe, F., Queloz, D., et al. 2003, Msngr, 114, 20
Meléndez, J., Ramírez, I., Karakas, A. I., et al. 2014, ApJ, 791, 14
Metcalfe, T. S., Finley, A. J., Kochukhov, O., et al. 2022, ApJL, 933, L17
Morgenthaler, A., Petit, P., Saar, S., et al. 2012, A&A, 540, A138
Noyes, R. W., Weiss, N. O., & Vaughan, A. H. 1984, ApJ, 287, 769
Oláh, K., Kővári, Z., Petrovay, K., et al. 2016, A&A, 590, A133
Olspert, N., Lehtinen, J. J., Käpylä, M. J., Pelt, J., & Grigorievskiy, A. 2018, A&A, 619, A6
Parker, E. N. 1955, ApJ, 122, 293
Petit, P., Dintrans, B., Solanki, S. K., et al. 2008, MNRAS, 388, 80
Porto de Mello, G. F., & da Silva, L. 1997, ApJL, 482, L89
Porto de Mello, G. F., da Silva, R., da Silva, L., & de Nader, R. V. 2014, A&A, 563, A52

Ramírez, I., Allende Prieto, C., Lambert, D. L., Koesterke, L., & Asplund, M. 2009, MmSAI, 80, 618

Rasmussen, C. E., & Williams, C. K. I. 2006, Gaussian Processes for Machine Learning (Berlin: Springer)

Reinhold, T., Cameron, R. H., & Gizon, L. 2017, A&A, 603, A52

Saar, S. H., & Brandenburg, A. 1999, ApJ, 524, 295

Sahlholdt, C. L., Feltzing, S., Lindegren, L., & Church, R. P. 2019, MNRAS, 482, 895

Sanderson, T. R., Appourchaux, T., Hoeksema, J. T., & Harvey, K. L. 2003, JGRA, 108, 1035

Scargle, J. D. 1982, ApJ, 263, 835

Schwabe, M. 1843, AN, 20, 283

Schwarz, G. 1978, AnSta, 6, 461

See, V., Jardine, M., Vidotto, A. A., et al. 2016, MNRAS, 462, 4442

Soubiran, C., & Triaud, A. 2004, A&A, 418, 1089

Stellingwerf, R. F. 1978, ApJ, 224, 953

Strassmeier, K. G. 2004, in IAU Symp. 219, Stars as Suns: Activity, Evolution and Planets, ed. A. K. Dupree & A. O. Benz (Cambridge: Cambridge Univ. Press), 11

Strugarek, A., Beaudoin, P., Charbonneau, P., Brun, A. S., & do Nascimento, J. D. 2017, Sci, 357, 185

Strugarek, A., Brun, A. S., Matt, S. P., & Réville, V. 2015, ApJ, 815, 111

Takeda, Y., Kawanomoto, S., Honda, S., Ando, H., & Sakurai, T. 2007, A&A, 468, 663

Tanner, A. M., Gelino, C. R., & Law, N. M. 2010, PASP, 122, 1195

Trilling, D. E., Bryden, G., Beichman, C. A., et al. 2008, ApJ, 674, 1086

VanderPlas, J. T. 2018, ApJS, 236, 16

Vaughan, A. H., Preston, G. W., & Wilson, O. C. 1978, PASP, 90, 267

Velloso, E. N., Anthony, F., do Nascimento, J.-D., et al. 2023, ApJL, 945, L12

Vogt, S. S., Allen, S. L., Bigelow, B. C., et al. 1994, Proc. SPIE, 2198, 362

Weiss, N. O., & Tobias, S. M. 2016, MNRAS, 456, 2654

Wilson, O. C. 1968, ApJ, 153, 221

Wilson, O. C. 1978, ApJ, 226, 379

Wright, J. T., Marcy, G. W., Butler, R. P., & Vogt, S. S. 2004, ApJS, 152, 261

Wu, Z., & Huang, N. E. 2009, Advances in Adaptive Data Analysis, 01, 1

Zaqarashvili, T. V., Oliver, R., Hanslmeier, A., et al. 2015, ApJL, 805, L14

Zechmeister, M., & Kürster, M. 2009, A&A, 496, 577